Energization of cold ions by electromagnetic ion cyclotron waves: Magnetospheric multiscale (MMS) observations

Cite as: Phys. Plasmas **28**, 072901 (2021); https://doi.org/10.1063/5.0046764
Submitted: 08 February 2021 . Accepted: 10 June 2021 . Published Online: 06 July 2021

A. A. Abid, Quanming Lu, X. L. Gao, B. M. Alotaibi, S. Ali, M. N. S. Qureshi, Y. Al-Hadeethi, and Shui Wang

Energization of cold ions by electromagnetic ion cyclotron waves: Magnetospheric multiscale (MMS) observations

Cite as: Phys. Plasmas **28**, 072901 (2021); doi: 10.1063/5.0046764
Submitted: 8 February 2021 · Accepted: 10 June 2021 ·
Published Online: 6 July 2021

View Online Export Citation CrossMark

A. A. Abid,[1,2,a)] Quanming Lu,[1] X. L. Gao,[1] B. M. Alotaibi,[3] S. Ali,[2] M. N. S. Qureshi,[4] Y. Al-Hadeethi,[5] and Shui Wang[1]

AFFILIATIONS

[1]CAS Key Laboratory of Geospace Environment, Department of Geophysics and Planetary Science, University of Science and Technology of China, Hefei 23006, China
[2]National Centre for Physics (NCP) at Quaid-e-Azam University Campus, Shahdra Valley Road, Islamabad 44000, Pakistan
[3]Department of Physics, College of Science, Princess Nourah Bint Abdulrahman University, Riyadh 11671, Saudi Arabia
[4]Department of Physics, GC University, Lahore 54000, Pakistan
[5]Department of Physics, Faculty of Sciences, King Abdulaziz University, Jeddah 21589, Saudi Arabia

Note: This paper is a part of the Special Collection: Plasma Physics from the Magnetospheric Multiscale Mission.
[a)]**Author to whom correspondence should be addressed:** abidaliabid1@hotmail.com

ABSTRACT

Electromagnetic ion cyclotron (EMIC) waves have been studied in this manuscript which are triggered by hot proton thermal anisotropy having energy ranging from 7 to 26 keV with a minimum resonant energy of 6.9 keV. However, an opposite effect can be observed for the hot protons for energy less than the minimum resonant energy. When the intensity of EMIC waves is large, the cold protons (ions) having low-energies can be energized by the EMIC waves. The possible reasons for this energization are the phase bunching of low energy ions with EMIC waves and the generation of electric fields at the relaxation time of substorm. As a consequence, these undetectable protons now become detectable, and the number density and temperature anisotropy of the protons also increase within the energy range from 1 to 100 eV. Accordingly, the helium ions are also energized by the EMIC waves.

I. INTRODUCTION

The electromagnetic ion cyclotron (EMIC) waves are generally detected in the Earth's magnetosphere and have a small wave normal angle and left-hand polarization in the source region.[1–3] These waves have large wave normal angle and linear polarization when they spread out from their source region due to the background magnetic field refraction.[4] The EMIC waves can be identified into three bands:[5,6] the H^+-band with the angular frequency (f) between the gyrofrequencies of the hydrogen and helium ions (i.e., $f_{cH+} > f > f_{cHe+}$), the He^+-band with the frequency between the gyrofrequencies of the helium and oxygen ions ($f_{cHe+} > f > f_{cO+}$), and the O^+-band with the frequency lower than the oxygen ion gyrofrequency ($f < f_{cO+}$). Here f_{cH^+}, f_{cHe^+}, and f_{cO^+} stand for the gyrofrequencies of H^+, H_e^+, and O^+ ions,[6,7] respectively.

EMIC waves have played a crucial role in the dynamics of the magnetosphere, for example, energizing of cold electrons as well as ions,[8,9] rapid loss of the radiation belt electrons because of pitch-angle (PA) scatterings,[10–15] precipitation of ions ring current,[16] etc. The activity of EMIC waves strongly increases in the plasmapause around the dusk side during the main storm phase. In the inner magnetospheric region where the energetic ions population overlaps the cold dense plasma, the electromagnetic ion–cyclotron waves are preferentially excited. The energetic ions are eventually lost into the atmosphere because of interactions with EMIC waves. Likewise, when the electrons reach the same zone, an interaction may take place with EMIC waves and (falling) moving down into the atmosphere.[17] The cold dense plasmas have also received a great deal of attention because of reducing the instability threshold to produce EMIC waves.[18] In several observational and theoretical findings, the generation of EMIC-waves occurs, when the hot anisotropic ions ($T_\perp > T_{||}$) come across the cold but dense plasmasphere.[19–21] The plasmaspheric plume structures[8] and solar wind high pressure[22,23] are preferred where the EMIC waves can easily be produced. The highest existence areas for He^+-

and H^+-bands for EMIC waves are 17:00 < MLT < 20:00, which have been studied[24] by using data from Akebono satellite. Later, the occurrence of He^+-, O^+-, and H^+-bands has been reported[3,6,21,25–28] by using data from different satellites.

In this article, we consider a one-particular event of Magnetospheric Multiscale (MMS1) satellite and show that the intensity and growth of H^+-band involving the EMIC waves increase gradually in the inner magnetosphere by decreasing the value of the L-shell. It is found that the H^+-band of EMIC waves can locally be excited by temperature anisotropy of hot protons (whose energy ranges from 7 to 26 keV). It is further assessed that cold protons especially within the energy range 1–100 eV can be energized by EMIC waves and consequently the density of cold protons can be increased. The main factors are the phase bunching of low-energy ions with EMIC waves and electrical fields produced when the substorm is relaxed. The manuscript is organized as follows: in Sec. II, we present an introduction to the MMS mission and data analysis technique. Section III describes the observational results and finally, a summary is provided in Sec. IV.

II. INSTRUMENTATION

The Instrumentation Magnetospheric Multiscale (MMS) spacecraft was launched in an elliptical equatorial orbit on March 12, 2015, with geocentric apogee and perigee of 12 R_E and 1.2 R_E, respectively.[29] Four MMS satellites form almost a regular tetrahedron structure with the same apparatuses. The first stage of the MMS satellite was concentrated on the dayside of the magnetopause. The plan was targeted for the formation of tetrahedral in the outer magnetosphere (with 9–12 R_E geocentric) through the separations between the spacecraft beginning from 160 and then reaching 40, 20, 10 km throughout the first to the sixth month during dusk to down scanning. The measurements were carried out by the MMS, which are found altered from that of the previous magnetospheric mission concerning accuracy and time resolution.[30] These high-time resolution measurements are comprised of particles, fields, and waves.[31]

In the current work, the measurement from numerous instruments of the MMS1 (https://lasp.colorado.edu/mms/sdc/public/about/browse-wrapper/) has been used. We have employed the short-time fast-Fourier-transform (FFT) technique on the inconsistent magnetic field (B) and electric field (E). The number of FFT input is 1200 and the step length input is 400. In survey mode, the measurement of magnetic field vector is provided by search-coil-magnetometer (SCM) at 32 samples per second. The electric field vector data are provided by electric-field-double-probe (EDP) at eight samples per second by using the slow mode data. The high-time resolution data are not available during this event. The wave properties, including ellipticity and wave normal angle, are measured using the FFT method. The EMIC wave events have been identified for a long time, which is more than 45 min. The wave events are categorized by the ion-gyrofrequency band. The survey data of Hot Plasma Composition Analyzer (HPCA)[32] are used to measure the pitch angle, different energy flux, and number densities. During the event, He^+ fluxes are negligible, so we have assumed that He^+ did not play an important role in the processes observed. To measure the solar wind pressure, OMNI[33] website (https://omniweb.gsfc.nasa.gov/) data are used, and for AE (auroral electrojet) and SYM-H[34] the World Data Center (WDC) for Geomagnetism, Kyoto (http://wdc.kugi.kyoto-u.ac.jp/) is used.

III. OBSERVATIONAL RESULTS

The EMIC wave event is captured by Magnetosphere Multiscale Spacecraft in the region $L \sim 6.3R_E - 7.3R_E$ and 13.2–13.7 MLT (magnetic local time) at high magnetic latitude (>8.6°) during 14:00–14:50 UT, on December 14, 2015. Figure 1 elucidates an overview of this event, including (a) solar wind dynamic (flow) pressure, (b) and (c) AE and SYM-H indices, respectively, (d) wave amplitude, (e) dynamic spectrogram of magnetic field, (f) dynamic spectra of electric field, (g) the normal angle, (h) the ellipticity (ϵ), (i) proton density, and (j) helium ion density. In panels (e) and (f), the dashed black and solid blue lines denote the gyrofrequency of the proton (f_{cH^+}) and helium (f_{cHe^+}), respectively. The solar wind dynamic pressure is plotted by using OMNI dataset for the same time range, and the resolution of solar wind dynamic pressure data is 1-min. The geomagnetic SYM-H and AE indices are plotted as Figs. 1(b) and 1(c) by using solar wind data from World Data Center (WDC) for Geomagnetism, Kyoto for 2015-12-14/14:00 to 2015-12-14/14:50:00. In the algorithm, $\epsilon(= -1,\ 0,\ \text{and}\ 1)$ stands for the left-hand, linear, and right-hand polarizations, respectively. The amplitude of EMIC waves increases gradually from 14:27:33 UT to 14:33:00 and 14:39:30 to 14:48:00, and this region is represented by the vertical red lines. This amplitude is obtained by the SCM instrument and it shows the strength of the fluctuation in (around) the dominant mode of the EMIC wave. Figures 1(e) and 1(f) clearly show that the single H^+-band of EMIC waves among the hydrogen and helium gyrofrequency is detected, when the satellite travels from $L \sim 7.3$ to $L \sim 6.0$. The intensity of waves exactly agrees with the amplitude of the waves. The EMIC waves have a maximum amplitude for $L < 6.4$. The wave normal angle $\theta < 28$ is revealed in Fig. 1(g). The ellipticity (ϵ) can be inspected from Fig. 1(h) showing that the proton band of EMIC waves has nearly linear polarization. Figures 1(i) and 1(j) determine the proton and helium ions' total (cold and hot) number of densities. It is observed that hydrogen ion number density increases with time and precisely agrees with the intensity of EMIC waves.

It is found that the minimum resonant energy of the EMIC wave mode is 6.9 keV during this event. The EMIC waves may have cyclotron interaction with protons having energy greater than 6.9 keV. Figures 2(a)–2(d) show the pitch angle spectrogram of H^+ with four different higher energy (energy greater than minimum resonance energy) ranges, i.e., [Fig. 2(a)] 7–10 keV, [Fig. 2(b)] 11–13 keV, [Fig. 2(c)] 14–17 keV, and [Fig. 2(d)] 20–26 keV as labeled are detected by the HPCA instrument. It is studied from Figs. 2(a)–2(d) that the PA around 0° and 180° decreases and then around 90° it increases. The pitch angle distributions given in Fig. 2 display clearly the temperature anisotropy of hot protons. The perpendicular and parallel temperature components $T_\perp$ and $T_{||}$ are enhanced for all types of ions due to heating but because of first adiabatic invariant, the perpendicular temperature increases faster than the parallel temperature, which is a major consequence in anisotropy of ion temperature ($T_\perp/T_{||}$).[35] Two main mechanisms have been suggested for the generation of ion temperature anisotropy as follows: (i) energetic plasma species from the plasma sheet at night are being pumped into the inner magnetosphere during the magnetic storms and substorms to achieve high-temperature anisotropy[36–39] and (ii) the increase in the dynamic pressure of solar wind can cause magnetospheric compression that can lead to the ions with drift shell splitting.[40] The drift shell splitting mechanism can establish temperature anisotropic in the dayside of the

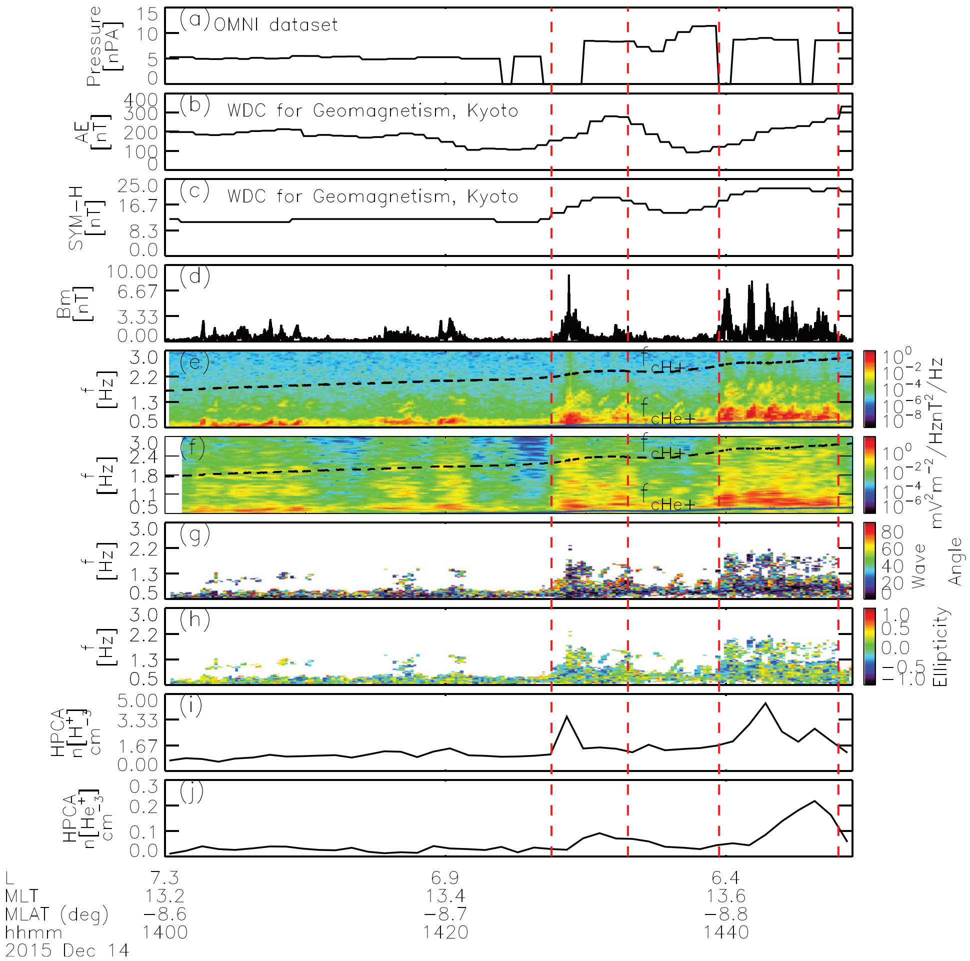

FIG. 1. The EMIC waves and their properties during an event (December 14, 2015) observed (a) solar wind dynamic (flow) pressure by OMNI dataset, (b) and (c) AE and SYM-H indices, respectively, by WDC for Geomagnetism, Kyoto, (d) amplitude of waves (B_m), (e) magnetic field wave power spectrogram of proton band EMIC waves, (f) electric field spectra, (g) wave-number angle, and (h) waves ellipticity as a function of frequency by using FFT (fast Fourier transform). (i) and (j) Hydrogen and helium ions total (hot and cold) number of densities, respectively, measured by MMS1.

magnetosphere. It is observed in Figs. 1(a)–1(c) that the trend of the dynamic pressure of solar wind, geomagnetic SYM-H, and AE indices is similar to the trend of amplitude, dynamic spectrogram of the magnetic field, and dynamic spectra of the electric field of EMIC waves. During the current event, the maximum value of AE index shows that there was an injection accompanied. The hot plasma species injected from the solar wind usually cause a temperature anisotropy and the increase in the dynamics of solar wind pressure will increase the temperature anisotropy. This ion's temperature anisotropy provides a free energy source for EMIC waves to grow.[1,25,41] Figure 2 clearly exhibits that as the temperature anisotropy increases the corresponding EMIC wave's spectra [shown by Figs. 1(e) and 1(f)] also increase. Figures 3(a)–3(d) show the pitch angles spectrogram of the protons within the energy range below the minimum resonant energy (6.9 keV). Figures 3(a) and 3(b) represent the PA of the cold proton with energy ranges 1–100 and 110–600 eV, respectively. It is observed that temperature anisotropy exists in cold ions especially in Fig. 3(a). It means that cold protons are energized by EMIC waves during this event and undetectable low-energy protons become detectable. Whereas opposite effects are observed in Figs. 3(c) and 3(d), where the energetic proton flux around the PA around 90° decreases. When EMIC waves modulate cold ions, the timescale of the change of cold ion energy approximates the period of the EMIC waves, as shown in a recent work.[42] This is because of the energetic protons with energy less than minimum resonant energy and having no cyclotron interaction with waves. By using HPCA, we measure the H^+ and He^+ distinctly in the energy range from 1 to 40 000 eV. The energy vs time spectrograms for H^+ and He^+ for differential energy fluxes are given in Figs. 4(a) and 4(b), respectively, indicating that protons are dominant during this event especially in the energy range 1–100 eV. The number density of cold protons (1–100 eV) and hot protons (7–26 keV) is illustrated in Figs. 4(c) and 4(d), and we find that the trend of cold proton number density is exactly the same as the total number density [as given in Fig. 1(e)]. One may justify it as that cold proton (1–100 eV) is energized by proton bands of EMIC waves. The other possibility could be the phase bunching of low-energy ions with EMIC waves at the time of onset of depolarization during the substorm time, which results in the energization in the radial direction. Another possibility could be the generation of large electric fields at the substorms expansion phase that may accelerate the low energy ions in the radial direction and result in the flat top distributions.[43,44] The kinetic energy shown in Fig. 4(f) for cold protons (1–100 eV) also represents almost a similar trend to protons number density and EMIC waves.

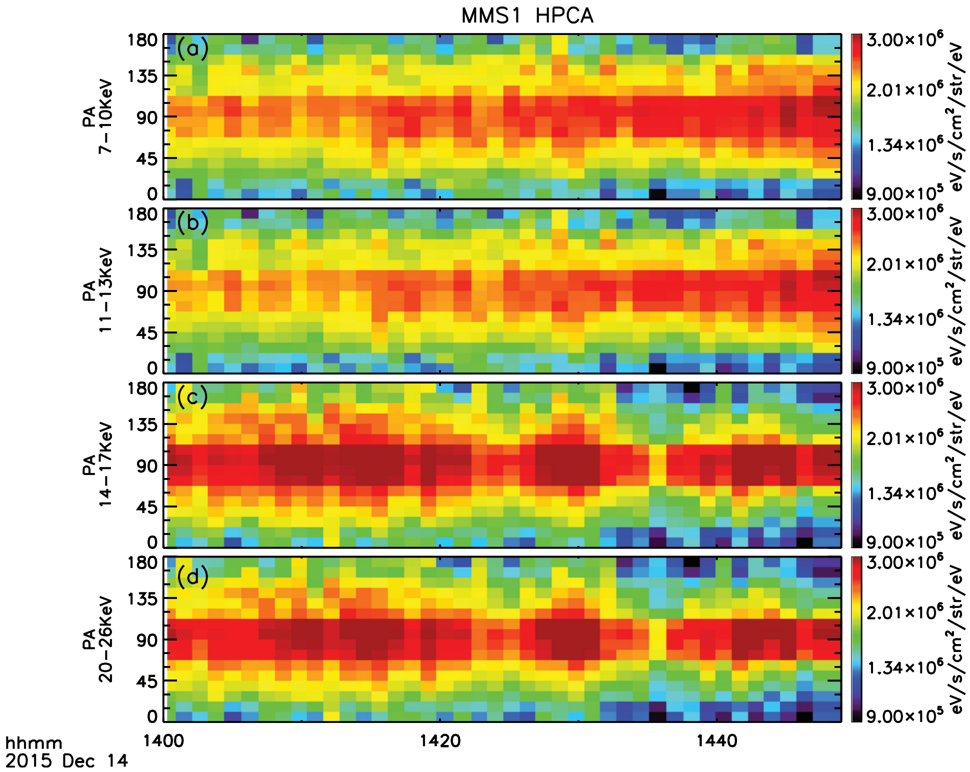

FIG. 2. Pitch angle (PA) distributions vs universal time (UT) of hydrogen ions for four different higher-energy ranges: (a) 7–10, (b) 11–13, (c) 14–17, and (d) 20–26 keV measured by Hot Plasma Composition Analyzer (HPCA) by the MMS1 spacecraft.

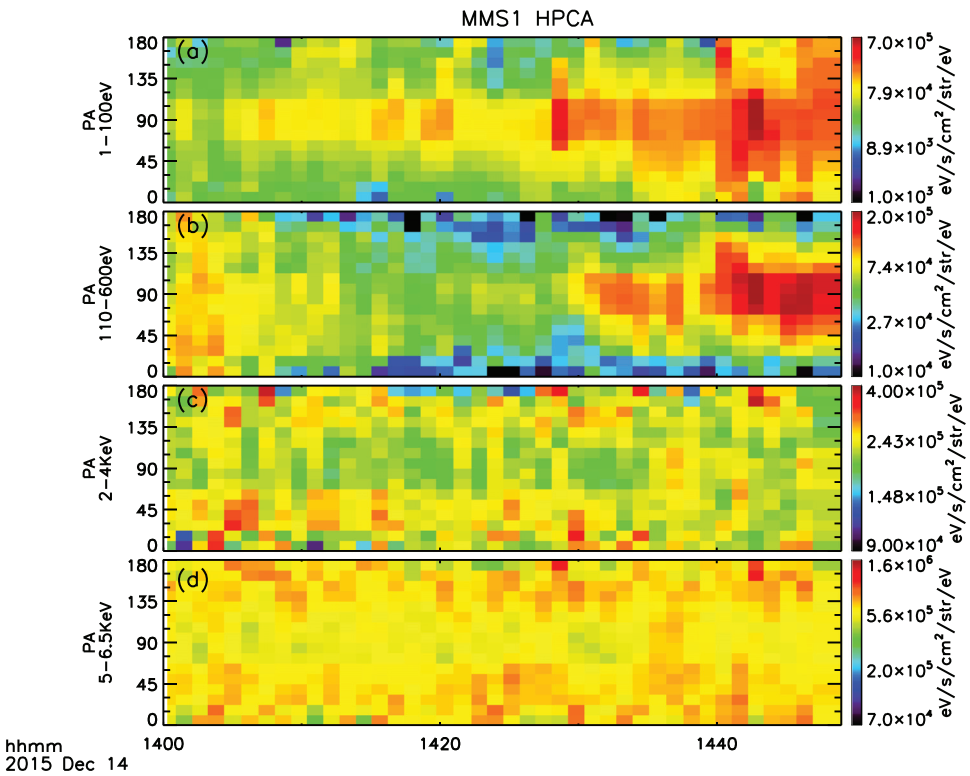

FIG. 3. Pitch angle (PA) distributions vs universal time (UT) of hydrogen ions for four different energy ranges: (a) 1–100, (b) 110–600, (c) 2–4, and (d) 5–6.5 keV measured by HPCA by the MMS1 spacecraft.

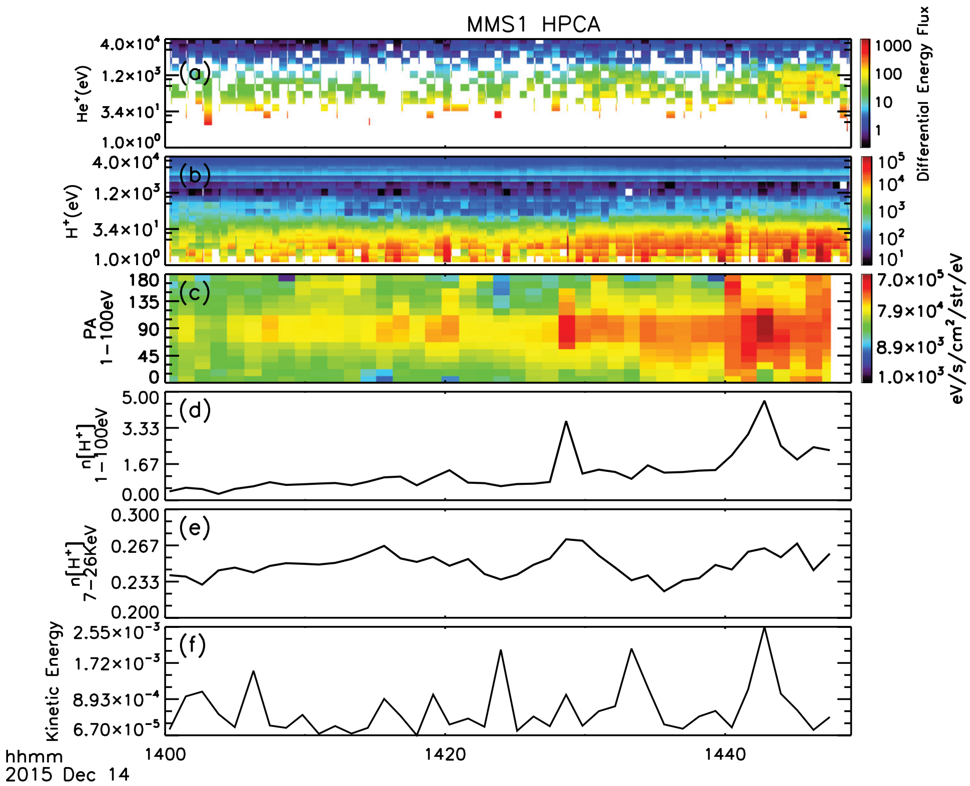

FIG. 4. Ion composition during the event: (a) and (b) different energy flux vs universal time for H^+ and He^+, respectively. (c) Pitch angle distribution with energy range 1–100 eV, (d) cold proton (1–100 eV) number density, (e) hot proton (7–26 keV) number density, and (f) kinetic energy of cold protons.

IV. SUMMARY

In summary, we have presented the EMIC wave event at 14:00–14:50 UT on December 14, 2015 measured by the Magnetospheric Multiscale (MMS1) spacecraft. In this event, the intensity and growth rate of the proton band involving the EMIC waves increase by decreasing the value of the L-shell. The maximum intensity of EMIC waves is located in the region $L < 6.4$, which corresponds to the dayside of the inner magnetosphere. The ellipticity and wavenumber angle elucidate that EMIC waves are expected nearby the source area. The hot anisotropic protons may excite the EMIC waves with energy greater than 6.9 keV and energetic ion temperature anisotropic provides the energy source for cyclotron instability in the generation of EMIC waves.[1,5,25,41] The enhancement of solar wind dynamic pressure leads to the temperature anisotropy of the hot plasma species in Earth's magnetosphere. EMIC waves are also located at a large value of L-shell in the noon sector, which means that the dynamic pressure of the solar wind is significant in the generation of EMIC waves as well because it can act like a cyclotron instability source.[22,23,45] The results display that protons are dominant species during this event, especially the energy range 1–100 eV [as shown in Fig. 4(b)]. It is assessed that the cold protons are energized by EMIC waves [Fig. 4(d)], and as a result of this energization, the cold protons are detectable. The possible reasons for this energization are the phase bunching of low energy ions with EMIC waves and the generation of electric fields at the relaxation time of substorm. It is now identified that mostly EMIC waves can occur near the plasmapause.[1] It is also noticed that the energization of cold proton number density is proportional to the EMIC wave's growth rate.

DATA AVAILABILITY

The data that support the findings of this study are available from the corresponding author upon reasonable request.

REFERENCES

1. R. Allen, J. C. Zhang, L. Kistler, H. Spence, R. L. Lin, B. Klecker, M. Dunlop, M. André, and V. Jordanova, J. Geophys. Res.: Space Phys. **120**(7), 5574–5592, https://doi.org/10.1002/2015JA021333 (2015).
2. Y. Liu, B. Fraser, and F. Menk, Geophys. Res. Lett. **39**(17), L17102, https://doi.org/10.1029/2012GL053082 (2012).
3. K. Min, J. Lee, K. Keika, and W. Li, J. Geophys. Res.: Space Phys. **117**(A5), A017515, https://doi.org/10.1029/2012JA017515 (2012).
4. L. Chen, V. K. Jordanova, M. Spasojević, R. M. Thorne, and R. B. Horne, J. Geophys. Res.: Space Phys. **119**(4), 2963–2977, https://doi.org/10.1002/2013JA019595 (2014).
5. J. M. Cornwall, J. Geophys. Res. **70**(1), 61–69, https://doi.org/10.1029/JZ070i001p00061 (1965).
6. X. Wang, S. Huang, R. Allen, H. Fu, X. Deng, M. Zhou, J. Burch, and R. Torbert, J. Geophys. Res.: Space Phys. **122**(8), 8228–8240, https://doi.org/10.1002/2017JA024237 (2017).
7. X. Yu, Z. Yuan, S. Huang, F. Yao, D. Wang, H. O. Funsten, and J. R. Wygant, Geophys. Res. Lett. **45**(3), 1271–1276, https://doi.org/10.1002/2018GL077109 (2018).
8. Z. Yuan, Y. Xiong, S. Huang, X. Deng, Y. Pang, M. Zhou, I. Dandouras, J. G. Trotignon, A. N. Fazakerley, and E. Lucek, Geophys. Res. Lett. **41**(6), 1830–1837, https://doi.org/10.1002/2014GL059241 (2014).
9. J. C. Zhang, L. Kistler, C. Mouikis, M. Dunlop, B. Klecker, and J. A. Sauvaud, J. Geophys. Res.: Space Phys. **115**(A6), 014030, https://doi.org/10.1029/2009JA014784 (2010).
10. R. B. Horne, R. M. Thorne, Y. Y. Shprits, N. P. Meredith, S. A. Glauert, A. J. Smith, S. G. Kanekal, D. N. Baker, M. J. Engebretson, and J. L. Posch, Nature **437**(7056), 227–230 (2005).

[11]G. Reeves, H. E. Spence, M. Henderson, S. Morley, R. Friedel, H. Funsten, D. Baker, S. Kanekal, J. Blake, and J. Fennell, Science **341**(6149), 991–994 (2013).
[12]M. Usanova, A. Drozdov, K. Orlova, I. Mann, Y. Shprits, M. Robertson, D. Turner, D. Milling, A. Kale, and D. Baker, Geophys. Res. Lett. **41**(5), 1375–1381, https://doi.org/10.1002/2013GL059024 (2014).
[13]J. Yu, L. Li, J. Cao, Z. Yuan, G. D. Reeves, D. Baker, J. Blake, and H. Spence, J. Geophys. Res.: Space Phys. **120**(12), 10275–10288, https://doi.org/10.1002/2015JA021460 (2015).
[14]L. Li, J. Yu, J. Cao, and Z. Yuan, Phys. Plasmas **23**(6), 062116 (2016).
[15]J. Yu, L. Li, J. Cui, J. Cao, J. Wang, Z. He, and J. Yang, J. Geophys. Res.: Space Phys. **125**(12), e2020JA028089, https://doi.org/10.1029/2020JA028089 (2020).
[16]Z. Yuan, Y. Xiong, Y. Pang, M. Zhou, X. Deng, J. G. Trotignon, E. Lucek, and J. Wang, J. Geophys. Res.: Space Phys. **117**(A3), A03205, https://doi.org/10.1029/2011JA017152 (2012).
[17]J. Rauch and A. Roux, J. Geophys. Res.: Space Phys. **87**(A10), 8191–8198, https://doi.org/10.1029/JA087iA10p08191 (1982).
[18]S. P. Gary, M. F. Thomsen, L. Yin, and D. Winske, J. Geophys. Res.: Space Phys. **100**(A11), 21961–21972, https://doi.org/10.1029/95JA01403 (1995).
[19]Z. Yuan, X. Deng, X. Lin, Y. Pang, M. Zhou, P. Décréau, J. Trotignon, E. Lucek, H. Frey, and J. Wang, Geophys. Res. Lett. **37**(7), L07108, https://doi.org/10.1029/2010GL042711 (2010).
[20]Y. Liu, S. Liu, and L. Zhou, Phys. Plasmas **20**(4), 043702 (2013).
[21]D. Wang, Z. Yuan, X. Yu, X. Deng, M. Zhou, S. Huang, H. Li, Z. Wang, Z. Qiao, and C. Kletzing, J. Geophys. Res.: Space Phys. **120**(6), 4400–4408, https://doi.org/10.1002/2015JA021089 (2015).
[22]M. Usanova, I. Mann, I. Rae, Z. Kale, V. Angelopoulos, J. Bonnell, K. H. Glassmeier, H. Auster, and H. Singer, Geophys. Res. Lett. **35**(17), L17S08, https://doi.org/10.1029/2010GL042711 (2008).
[23]J. McCollough, S. Elkington, and D. Baker, J. Geophys. Res.: Space Phys. **117**(A1), 15225, https://doi.org/10.1029/2011JA016948 (2012).
[24]Y. Kasahara, A. Sawada, M. Yamamoto, I. Kimura, S. Kokubun, and K. Hayashi, Radio Sci. **27**(02), 347–362, https://doi.org/10.1029/91RS01872 (1992).
[25]M. Usanova, I. Mann, J. Bortnik, L. Shao, and V. Angelopoulos, J. Geophys. Res.: Space Phys. **117**(A10), A10218, https://doi.org/10.1029/2012JA018049 (2012).
[26]N. P. Meredith, R. B. Horne, T. Kersten, B. J. Fraser, and R. S. Grew, J. Geophys. Res.: Space Phys. **119**(7), 5328–5342, https://doi.org/10.1002/2014JA020064 (2014).
[27]X. Yu, Z. Yuan, D. Wang, H. Li, S. Huang, Z. Wang, Q. Zheng, M. Zhou, C. Kletzing, and J. Wygant, Geophys. Res. Lett. **42**(5), 1312–1317, https://doi.org/10.1002/2015GL063250 (2015).
[28]R. Allen, J. C. Zhang, L. Kistler, H. Spence, R. L. Lin, B. Klecker, M. Dunlop, M. André, and V. K. Jordanova, J. Geophys. Res.: Space Phys. **121**(7), 6458–6479, https://doi.org/10.1002/2016JA022541 (2016).
[29]J. Burch, T. Moore, R. Torbert, and B. Giles, Space Sci. Rev. **199**(1–4), 5–21 (2016).
[30]C. Pollock, T. Moore, A. Jacques, J. Burch, U. Gliese, Y. Saito, T. Omoto, L. Avanov, A. Barrie, and V. Coffey, Space Sci. Rev. **199**(1–4), 331–406 (2016).
[31]M. Hesse, N. Aunai, J. Birn, P. Cassak, R. Denton, J. Drake, T. Gombosi, M. Hoshino, W. Matthaeus, and D. Sibeck, Space Sci. Rev. **199**(1–4), 577–630 (2016).
[32]D. Young, J. Burch, R. Gomez, A. De Los Santos, G. Miller, P. Wilson, N. Paschalidis, S. Fuselier, K. Pickens, and E. Hertzberg, Space Sci. Rev. **199**(1–4), 407–470 (2016).
[33]M. Vokhmyanin, N. Stepanov, and V. Sergeev, Space Weather **17**(3), 476–486, https://doi.org/10.1029/2018SW002113 (2019).
[34]P. Newell and J. Gjerloev, J. Geophys. Res.: Space Phys. **116**(A12), A12303, https://doi.org/10.1029/2011JA016779 (2011).
[35]J. V. Olson and L. Lee, Planet. Space Sci. **31**(3), 295–302 (1983).
[36]J. M. Cornwall and M. Schulz, J. Geophys. Res. **76**(31), 7791–7796, https://doi.org/10.1029/JA076i031p07791 (1971).
[37]S. Liu, Z. Xia, L. Chen, Y. Liu, Z. Liao, and H. Zhu, Geophys. Res. Lett. **46**(13), 7096–7104, https://doi.org/10.1029/2019GL083421 (2019).
[38]K. H. Kim, Y. Omura, H. Jin, and J. Hwang, J. Geophys. Res.: Space Phys. **122**(3), 3322–3341, https://doi.org/10.1002/2016JA023391 (2017).
[39]B. Remya, B. Tsurutani, R. Reddy, G. Lakhina, and R. Hajra, J. Geophys. Res.: Space Phys. **120**(9), 7536–7551, https://doi.org/10.1002/2015JA021327 (2015).
[40]D. Sibeck, J. Geophys. Res. **92**, 13485, https://doi.org/10.1029/JA092iA12p13485 (1987).
[41]M. Engebretson, J. Posch, N. Capman, N. Campuzano, P. Bělik, R. Allen, S. Vines, B. Anderson, S. Tian, and C. A. Cattell, J. Geophys. Res.: Space Phys. **123**(10), 8331–8357, https://doi.org/10.1029/2018JA025984 (2018).
[42]C. Shi, J. Zhao, C. Huang, T. Wang, and M. W. Dunlop, Phys. Plasmas **27**(3), 032902 (2020).
[43]D. Delcourt, J. A. Sauvaud, and T. Moore, J. Geophys. Res.: Space Phys. **102**(A11), 24313–24324, https://doi.org/10.1029/97JA02039 (1997).
[44]M. Qureshi, W. Nasir, R. Bruno, and W. Masood, Mon. Not. R. Astron. Soc. **488**(1), 954–964 (2019).
[45]M. Hellberg, R. Mace, T. Baluku, I. Kourakis, and N. Saini, Phys. Plasmas **16**(9), 094701 (2009).